

1 INTRODUCTION

2 Above Earth's atmosphere are the Van Allen radiation belts, a toroidally-shaped
3 pair of belts that consist of a complex and dynamic plasma environment. The inner
4 radiation belt is stable, consists of mostly energetic protons, and is located within 2
5 Earth radii (measured near the equator) above Earth's surface. The outer radiation
6 belt, on the other hand, consists of mostly energetic electrons, is highly dynamic
7 on day and hour time scales, and is typically found between 4 and 8 Earth radii
8 above Earth's surface. These belts pose a threat to space exploration due to their
9 adverse effects on our bodies and electrical components. A few **effects** include: a
10 high radiation dose for manned missions, degradation of silicon that causes transistor
11 malfunction, computer memory corruption due to bit flips, etc. With these effects in
12 mind, it is no surprise that the radiation belts have been extensively studied since
13 their discovery in the 1960s.

14 The radiation belt particles, mostly consisting of electrons and protons, are at
15 times unstable to wave growth and generate electric and magnetic waves. These
16 waves can then accelerate and scatter radiation belt particles with a variety of wave-
17 particle mechanisms. These wave-particle interactions are believed to be responsible
18 for scattering electron microbursts, a short and intense increase of precipitating
19 electrons into Earth's atmosphere, that are capable of destroying ozone molecules
20 and rapidly deplete the outer belt's electrons.

21 Electron microbursts, henceforth referred to as microbursts, are typically
22 observed by low Earth orbiting spacecraft, sounding rockets, and high altitude
23 balloons as a sub-second impulse of electrons. Some of the most intense microbursts
24 have electron fluxes that are a factor of 10 to 100 above the background (for example
25 see Fig. 7 in Blake et al. (1996)). Since they were first reported by Anderson and

26 Milton (1964), the intense transient nature of microbursts have compelled countless
27 researchers to pursue an understanding of their properties, their effects on the
28 environment, and the physical mechanism(s) that create microbursts. Microbursts
29 are widely believed to be created by wave-particle scattering between a plasma wave
30 called whistler mode chorus and outer radiation belt electrons, although many details
31 regarding the scattering mechanism are unconstrained or unknown. The goal of this
32 dissertation is to expand our knowledge of the wave-particle scattering mechanism
33 that scatters electron microbursts.

34 This chapter serves as an introduction to the fundamental physical concepts
35 that are essential to understand wave-particle interactions in Earth's magnetosphere.
36 We will review the motion of charged particles in electric and magnetic fields, how
37 particles are organized in the magnetosphere, how particles are accelerated and lost in
38 the magnetosphere, and review the current state of our understanding of microbursts.

39 Then the rest of this dissertation expands our knowledge of microbursts. In
40 Chapter ?? (chapter numbers will be filled in the full dissertation) we will investigate
41 and model the scattering mechanism responsible for microbursts observed inside the
42 outer radiation belt, near the magnetic equator. Then in Chapters ?? and ?? we
43 will investigate the microburst scattering mechanism indirectly by estimating the
44 microburst footprint size in low Earth orbit and the magnetic equator (near where
45 microburst electrons are believed to be scattered) and compare it to sizes of chorus
46 waves estimated in prior literature.

47 Charged Particle Motion in Electric and Magnetic Fields

A charged particle trapped in the magnetosphere will experience three types of periodic motion in Earth's nearly dipolar magnetic field in the absence of electric fields. The three motions are ultimately due to the Lorentz force that a particle of

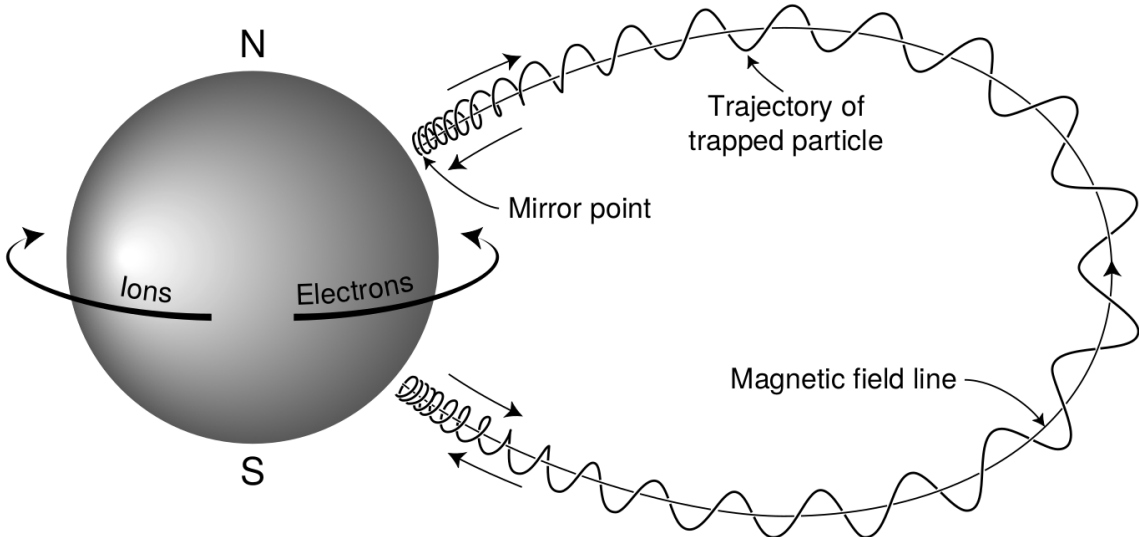


Figure 1.1: The three periodic motions of charged particles in Earth's dipole magnetic field. These motions are: gyration about the magnetic field line, bounce motion between the magnetic poles, and azimuthal drift around the Earth. Figure from (Baumjohann and Treumann, 1997).

momentum \vec{p} , charge q , and velocity \vec{v} experiences in an electric field \vec{E} and magnetic field \vec{B} and is given by

$$\frac{d\vec{p}}{dt} = q(\vec{E} + \vec{v} \times \vec{B}). \quad (1.1)$$

- ⁴⁸ In the magnetosphere, the three periodic motions, in decreasing frequency, are
- ⁴⁹ gyration, bounce, and drift and are schematically shown in Fig. 1.1. Each periodic
- ⁵⁰ motion has a corresponding conserved quantity i.e. an adiabatic invariant.

The highest frequency periodic motion is gyration about a magnetic field of magnitude B . This motion is circular with a Larmor radius of

$$r = \frac{mv_{\perp}}{|q|B} \quad (1.2)$$

where m is the mass and v_{\perp} the particle's velocity perpendicular to \vec{B} . This motion

has a corresponding gyrofrequency of

$$\Omega = \frac{|q|B}{m} \quad (1.3)$$

in units of radians/second. In the radiation belts, the electron gyrofrequency, Ω_e , is on the order of a kHz. The corresponding adiabatic invariant is found by integrating the particle's canonical momentum around the particle's path of gyration,

$$J_i = \oint (\vec{p} + q\vec{A}) \cdot d\vec{l} \quad (1.4)$$

where J_i is the i^{th} adiabatic invariant and \vec{A} is the magnetic vector potential. This integral is carried out by integrating the first term over the circumference of the gyro orbit and integrating the second term using Stokes theorem to calculate the magnetic flux enclosed by the gyro orbit. The gyration invariant is $J_1 \sim v_\perp^2/B$ which is conserved when the frequency, ω , of a force acting on the gyrating electron satisfies

$$\omega \ll \Omega_e.$$

The second highest frequency periodic motion is bouncing due to a parallel gradient in \vec{B} . This periodic motion naturally arises in the magnetosphere because Earth's magnetic field is stronger near the poles. To understand this motion we first we need to define the concept of pitch angle, α as the angle between \vec{B} and \vec{v} which is schematically shown in Fig. 1.2a. The pitch angle relates v with v_\perp and $v_{||}$, the component of the particles velocity parallel to \vec{B} . As shown in Fig. 1.2b and 1.2c, a smaller (larger) α will increase (decrease) the distance that the charged particle travels parallel to \vec{B} during one gyration.

Assuming the particle's kinetic energy is conserved, the conservation of J_1 implies that given a particle's $v_\perp(0)$ and $B(0)$ at the magnetic equator (where Earth's magnetic field is usually at a minimum) we can calculate its $v_\perp(s)$ along

the particle's path, s , by calculating $B(s)$ from magnetic field models. Thus the particle's perpendicular velocity is then related via

$$\frac{v_{\perp}^2(0)}{B(0)} = \frac{v_{\perp}^2(s)}{B(s)} \quad (1.5)$$

⁶⁵ which can be rewritten as

$$\frac{v^2 \sin^2 \alpha(0)}{B(0)} = \frac{v^2 - v_{\parallel}^2(s)}{B(s)} \quad (1.6)$$

⁶⁶ and re-arranged to solve for $v_{\parallel}(s)$ by

$$v_{\parallel}(s) = v \sqrt{1 - \frac{B(s)}{B(0)} \sin^2 \alpha(0)} \quad (1.7)$$

⁶⁷ which will tend towards 0 as the second term in the radical approaches 1.

⁶⁸ The location where $v_{\parallel}(s) = 0$ is called the mirror point and is where a particle
⁶⁹ reverses direction. Since Earth's magnetic field is stronger towards the poles, the
⁷⁰ mirroring particle will execute periodic bounce motion between its two mirror points
⁷¹ in the northern and southern hemispheres. The corresponding adiabatic invariant, J_2
⁷² is

$$J_2 = \oint p_{\parallel} ds \quad (1.8)$$

where ds describes the particle path between the mirror points in the northern and southern hemispheres (see Fig. 1.1). J_2 is found by substituting Eq. 1.7 into Eq. 1.8 and defining the magnetic field strength at the mirror points as B_m (where $\alpha(m) = 90^\circ$). The J_2 integral can be written as

$$J_2 = 2p \int_{m_n}^{m_s} \sqrt{1 - \frac{B(s)}{B(m)}} ds \quad (1.9)$$

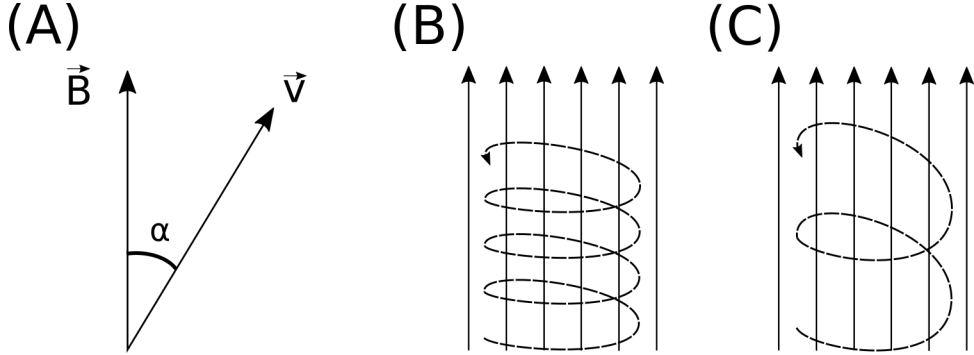


Figure 1.2: Charged particle motion in a uniform magnetic field \vec{B} . Panel (A) shows the geometry defining the pitch angle, α . Panel (B) and (C) show two helical electron trajectories with dashed lines assuming a large and small α (corresponding to a small and large parallel velocity $v_{||}$), respectively.

73 where m_n and m_s are the northern and southern mirror points, respectively. The
 74 bounce period can be estimated (e.g. Baumjohann and Treumann, 1997) to be

$$t_b \approx \frac{LR_e}{\sqrt{W/m}}(3.7 - 1.6 \sin \alpha(0)) \quad (1.10)$$

75 where W is the particle's kinetic energy, and L is the L -shell. The L -shell is the
 76 distance from the Earth's center to the location where a particular magnetic field
 77 line crosses the magnetic equator, in units of Earth radii, R_e . As with gyration, the
 78 particle will bounce between the mirror points as long as $\omega \ll \Omega_b$, where Ω_b is the
 79 bounce frequency.

80 At this stage it is instructional to introduce loss cone pitch angle, α_L .
 81 Conventionally, the loss cone pitch angle is defined as the pitch angle where a particle
 82 will mirror at ≈ 100 km altitude in the atmosphere. A charged particle gyrating at
 83 those altitudes will encounter and Coulomb scatter with the dense atmosphere and
 84 be lost. The 100 km altitude is only a convention and not a hard boundary, e.g. the
 85 peak in the 1 MeV electron ionization rate is at ≈ 60 km altitudes (Fang et al., 2010).

86 The slowest periodic motion experienced by charged particles in Earth's

87 magnetic field is azimuthal drift around the Earth. This drift primarily results from
 88 a combination of a radial gradient in \vec{B} and the curvature of the magnetic field. The
 89 radial gradient drift arises because Earth's magnetic field is stronger near the Earth.
 90 The particle's gyroradius shrinks as it gyrates towards Earth, and expands when it
 91 gyrates away from Earth. The overall effect is the particle gyro orbit does not close
 92 on itself causing eastward drift of negatively charged particles and westward drift
 93 of positively charged particles. The radial gradient drift is further enhanced by the
 94 centrifugal force that a particle experiences as it bounces along the curved field lines.
 95 The drift adiabatic invariant, J_3 is found by integrating Eq. 1.4 over the complete
 96 particle orbit around the Earth. The shape of this drift orbit is known as a drift shell,
 97 and can be visualized by rotating the trapped particle trajectory in Fig. 1.1 around
 98 the axis that connects the poles. For J_3 , the first term is negligible and the second
 99 term is the magnetic flux enclosed by the drift shell, Φ_m i.e. $J_3 \sim \Phi_m$ Add the J_3
 100 derivation.

101 To quantify the frequencies of the three periodic motions, Fig. 1.3 from Schulz
 102 and Lanzerotti (1974) shows contours of the gyration, bounce, and drift frequencies
 103 for electrons and protons in Earth's dipole magnetic field.

Up until now we have considered the three periodic motions due Earth's magnetic field in the absence of electric fields. If there is an electric field, \vec{E} , perpendicular to \vec{B} , a particle's center of gyration (averaged position of the particle over a gyration) will drift with a velocity perpendicular to both \vec{E} and \vec{B} . The drift velocity can be solved using Eq. 1.1 and is

$$\vec{v}_E = \frac{\vec{E} \times \vec{B}}{B^2}. \quad (1.11)$$

104 If there is a parallel magnetic field, $E_{||}$, then the particle is accelerated along the
 105 magnetic field line. An $E_{||}$ pointing away from the Earth will contribute to the mirror

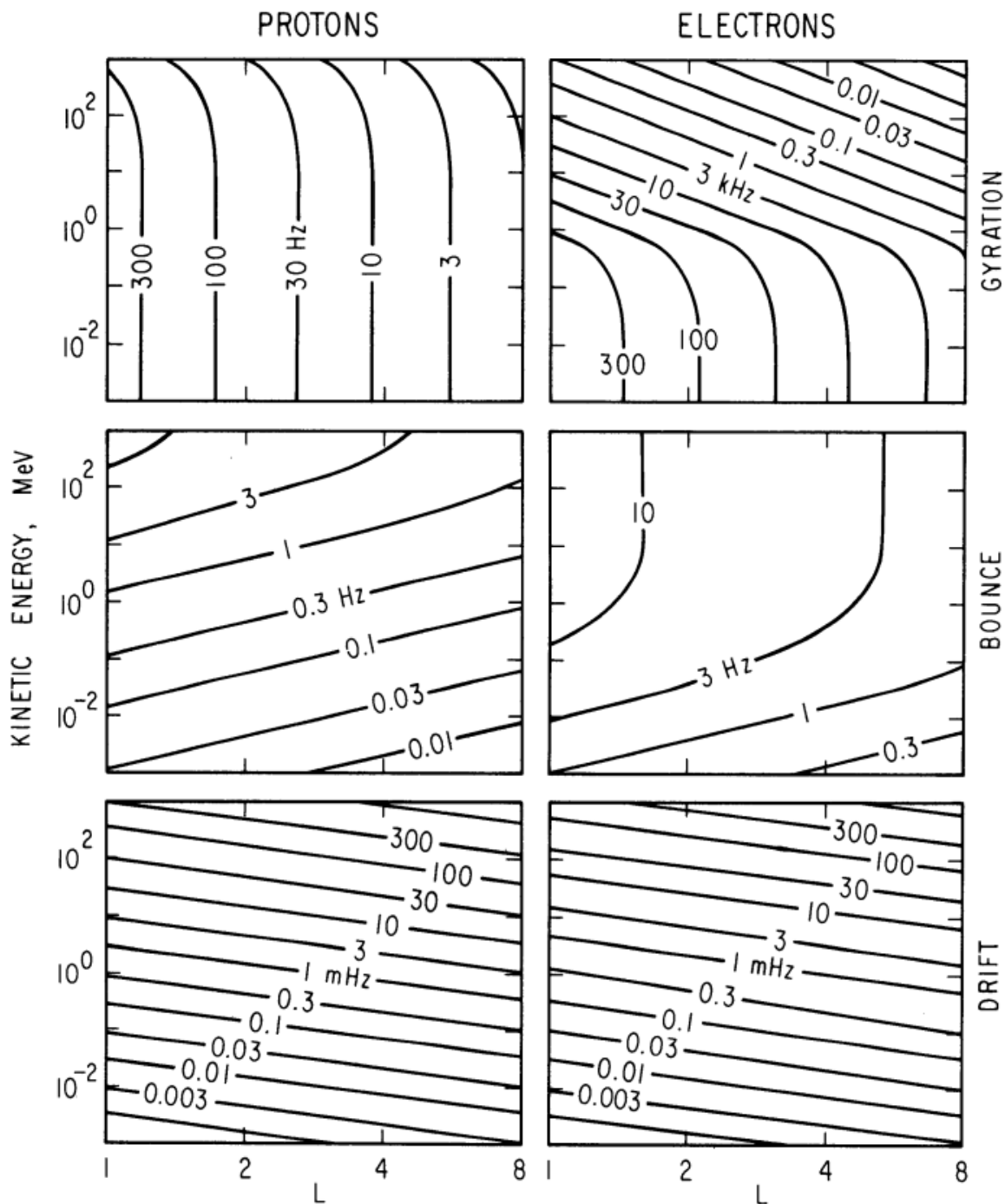


Figure 1.3: Contours of constant gyration, bounce, and drift frequencies for electrons and protons in a dipole field. Figure from Schulz and Lanzerotti (1974).

106 force and raise the particle's mirror point. On the contrary, an Earthward pointing
 107 $E_{||}$ will oppose the mirror force and lower the mirror point. If the Earthward $E_{||}$
 108 lowers the mirror point into the atmosphere, those particles will precipitate into the
 109 atmosphere. This is the mechanism that generates the aurora.

110 Particle Populations and Their Interractions in the Magnetosphere

111 Now that we have looked at the dynamics of single-particle motion in electric
 112 and magnetic fields, we will briefly tour the various macroscopic populations in the
 113 magnetosphere that are illustrated in Fig. 1.4.

114 The sun and its solar wind are ultimately the source of energy input into the
 115 magnetosphere. The solar wind at Earth's orbit is a plasma traveling at supersonic
 116 speeds with an embedded interplanetary magnetic field (IMF). When the solar wind
 117 encounters Earth's magnetic field, the plasma can not easily penetrate into the
 118 magnetosphere because the plasma is frozen-in on magnetic field lines. The plasma
 119 is frozen-in on magnetic field lines because plasma has a nearly infinite conductivity.
 120 Thus the plasma and its magnetic field drapes around the magnetosphere, forming a
 121 cavity in the solar wind that qualitatively has a shape as shown in Fig. 1.4. The solar
 122 wind is supersonic at 1 AU so a bow shock exists upstream of the magnetosphere
 123 which compresses and heats the solar wind. Downstream of the bow shock, the
 124 solar wind plasma flows around the magnetosphere inside the magnetosheath. The
 125 magnetopause is the surface where the solar wind ram and Earth's magnetic pressures
 126 balance. To first order, the magnetopause can be thought of as a boundary between
 127 the solar wind and Earth's magnetosphere. The shocked plasma then flows past the
 128 Earth where it shapes the magnetotail. In the magnetotail, the magnetopause exists
 129 where the solar wind magnetic pressure balances Earth's magnetic field pressure in
 130 the lobes. The magnetotail extends on the order of 100 R_E downstream of Earth,

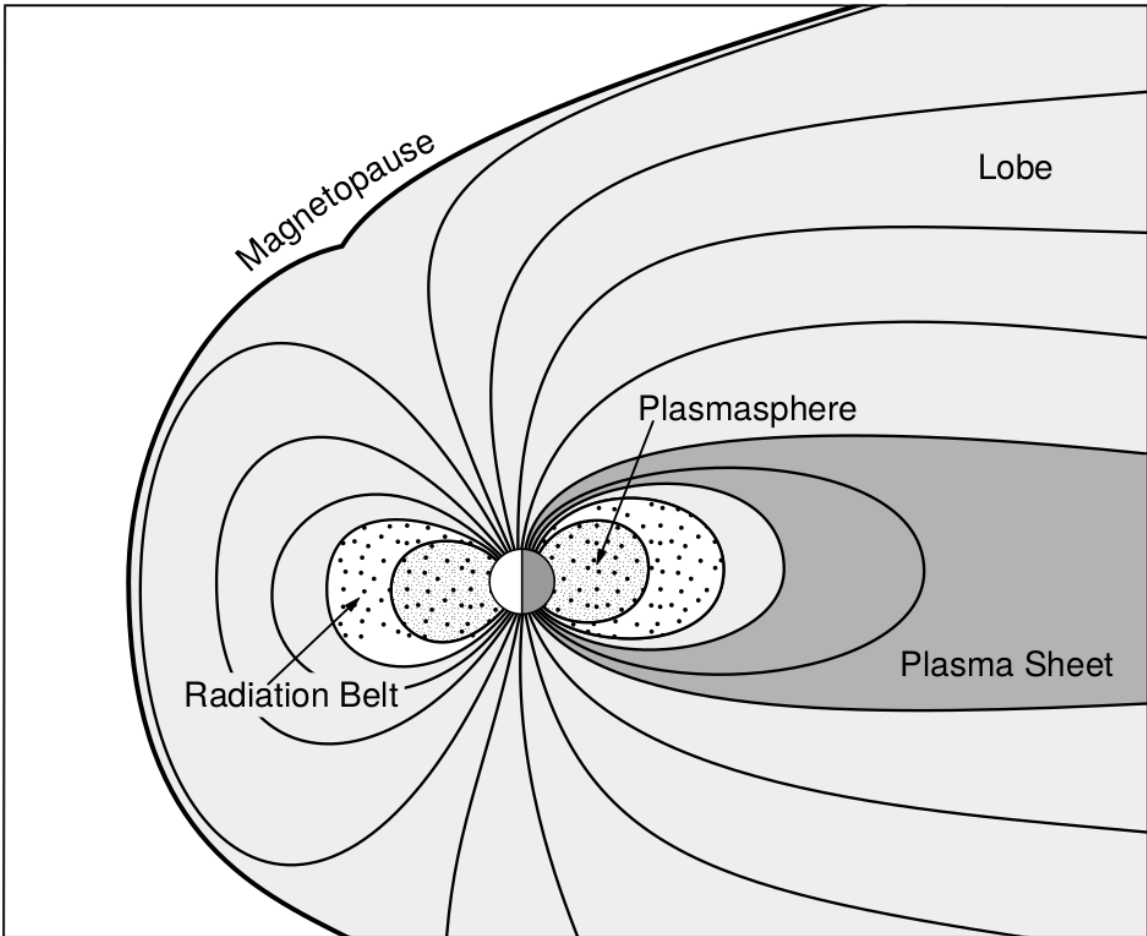


Figure 1.4: A few macroscopic structures in the magnetosphere. The magnetosphere boundary with the solar wind is the magnetopause. The magnetotail consists of two lobes that contain Earth's magnetic flux with the plasma sheet separating the two lobes. The inner magnetosphere contains the plasmasphere, the ring current, and the radiation belts which are co-located. Figure from Baumjohann and Treumann (1997).

and the tailward stretching of magnetic field lines creates a region where Earth's Earthward and anti-Earthward magnetic fields are in proximity. In this region, the curl of \vec{B} is non-zero, thus by Ampere's law there must be a current (called the plasma sheet) near the magnetic equator (e.g. Eastwood et al., 2015).

Populations in the Inner Magnetosphere

Closer to Earth, where the magnetic field is largely dipolar, are three plasma populations that comprise the inner magnetosphere: the plasmasphere, the ring current, and the radiation belts which are shown in Fig. 1.4. Before we describe these three particle populations in detail, we will first introduce the coordinate system that most naturally describes the inner magnetosphere environment, and then the electric fields that effect mostly low energy particles.

In this coordinate system the “radial” coordinate was defined in section 1 and is the L shell. The azimuthal coordinate is the magnetic local time (MLT). For an observer above Earth's north pole looking down, MLT is defined to be 0 (midnight) in the anti-sunward direction, and increases in the counter-clockwise direction with 6 at dawn, 12 at noon (sunward direction), and 18 in dusk. The final coordinate is the magnetic latitude, λ which is analogous to the latitude coordinate in the spherical coordinate system, and is defined to be 0 at the magnetic equator. This coordinate system is shown in Fig. 1.5 and naturally describes the inner magnetosphere populations described below.

The low energy particle dynamics in the inner magnetosphere are organized by two electric fields: the co-rotation and the dawn-dusk electric fields. The co-rotation electric field arises from Earth's rotation. The magnetic field and the particles frozen on it rotate with the Earth. To a non-rotating observer this rotation appears as a radial electric field that drops off as $\sim L^{-2}$. The other electric field, pointing from

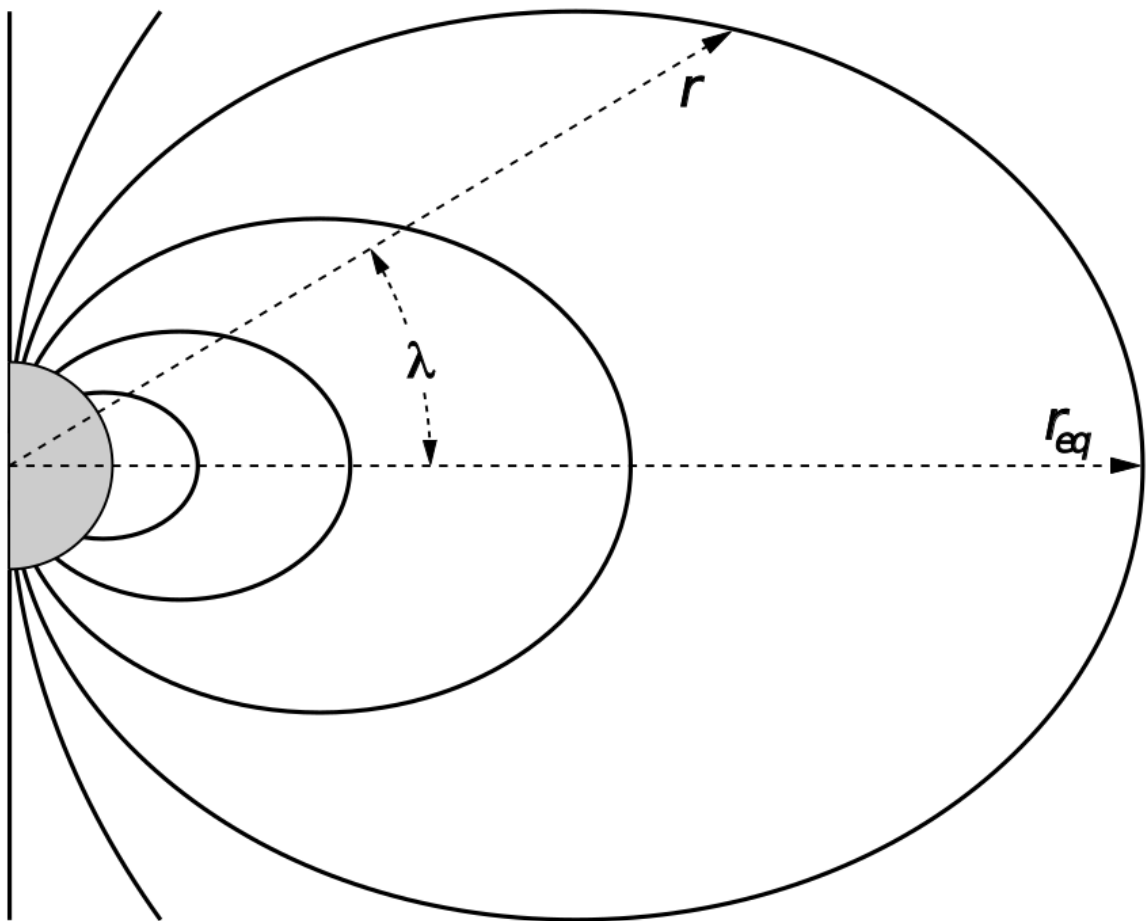


Figure 1.5: The dipole coordinate system. The magnetic latitude of \mathbf{r} is λ . The radial distance to a magnetic field line in the equatorial plane is typically given by $L = r_{eq}/R_e$. Figure from Baumjohann and Treumann (1997).

156 dawn to dusk is called the convection electric field and is due to the Earthward
 157 transport of particles from the magnetotail that appears as an electric field in Earth's
 158 reference frame. The superposition of the co-rotation and and convection electric
 159 fields is a potential field shown in Fig. 1.6. The shaded area in Fig. 1.6 shows the
 160 orbits on which low energy electrons are trapped, and outside this region the particles
 161 are not trapped. The dynamic topology of the shaded region in Fig. 1.6 is controlled
 162 by only the convection electric field which is dependent on the solar wind speed and
 163 the IMF. The lowest energy particles that orbit in the shaded region in Fig. 1.6 make
 164 up the plasmasphere.

165 Plasmasphere The plasmasphere is a dense ($n_e \sim 10^3/\text{cm}^3$), cool ($\sim \text{eV}$)
 166 plasma. The plasmasphere typically extends to $L \sim 4$ and the spatial extent is
 167 highly dependent on the solar wind and magnetospheric conditions. The source
 168 of the plasmasphere is the ionosphere. The two main mechanisms that fill the
 169 plasmasphere with cold plasma are ionization of the ionosphere by sunlight and
 170 particle precipitation. The ultraviolet ionization by sunlight is strongly dependent
 171 on the time of day (day vs night), latitude (more ionization near the equator). The
 172 ionization due to particle precipitation, on the other hand, is highly dependent on
 173 magnetospheric conditions, and mostly occurs at high latitudes.

174 The outer boundary of the plasmasphere is the plasmapause which is typically
 175 identified as a steep radial gradient in plasma density from $\sim 10^3/\text{cm}^3$ to $\sim 1/\text{cm}^3$.
 176 The location of the plasmapause is important to model (e.g. O'Brien and Moldwin,
 177 2003) and understand since the plasma density strongly controls the efficiency of
 178 particle scattering by waves (e.g. Horne et al., 2005).

179 Ring Current The next higher energy population is the ring current. This
 180 population consists of protons and electrons between tens and a few hundred keV

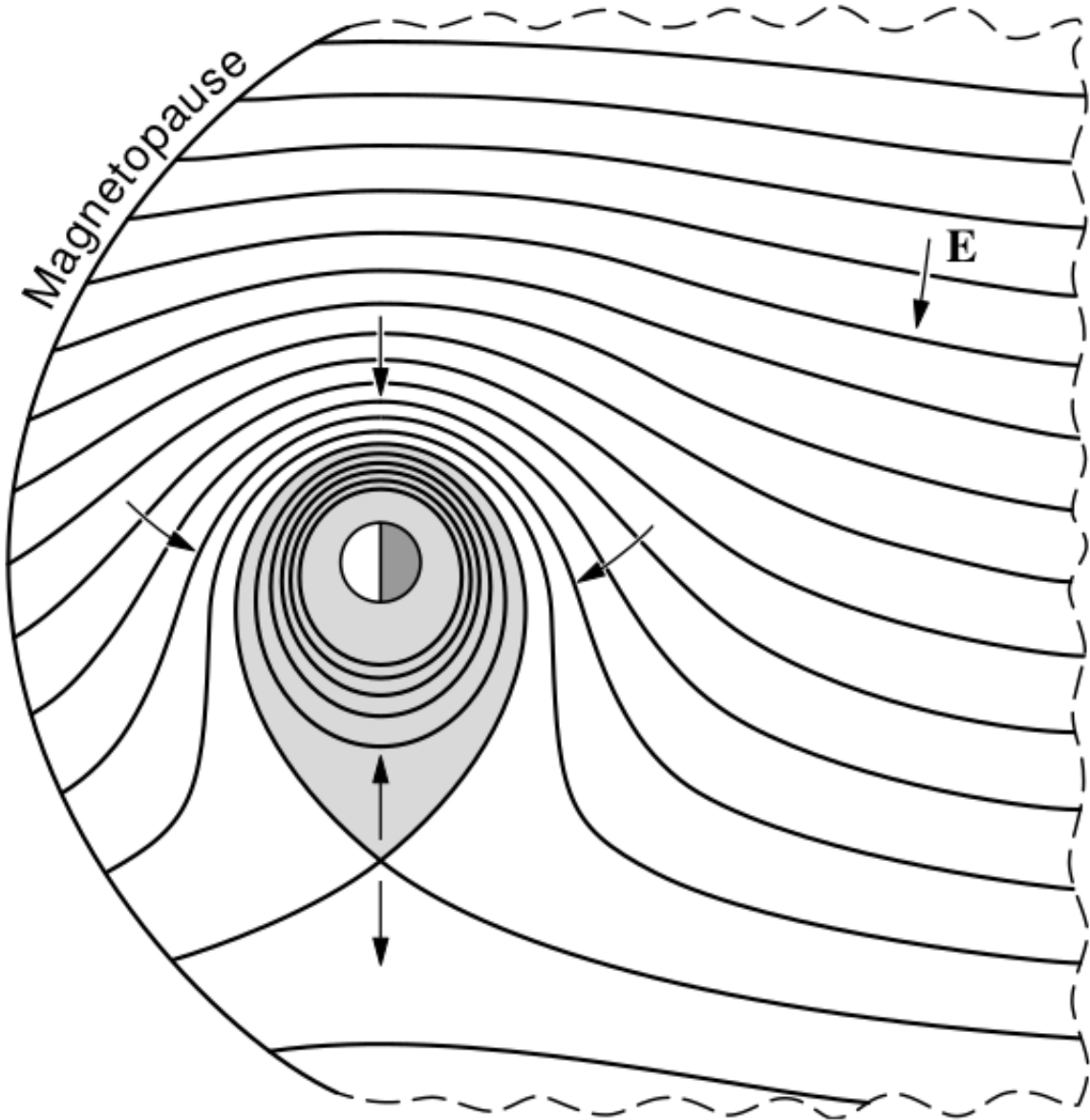


Figure 1.6: Equipotential lines and electric field arrows due to the superposition of the co-rotation and convection electric fields. Electrons in the shaded region execute closed orbits. Outside of the shaded regions the electrons are not trapped and will escape. The region separating the two regimes is called the Alfvén layer. Figure from Baumjohann and Treumann (1997).

181 that drift around the Earth. The orbits of higher energy particles are not as effected
182 by the convection and co-rotation electric field, rather they drift around the Earth
183 due to gradient and curvature drifts. Since the direction of the drift is dependent on
184 charge, protons drift west around the Earth and electrons drift East. This has the
185 effect of creating a current around the Earth.

186 The ring current generates a magnetic field which decreases the magnetic field
187 strength at the surface of the Earth and increases it outside of the ring current.
188 The decrease of Earth's magnetic field strength is readily observed by a system of
189 ground-based magnetometers and is merged into a Disturbance Storm Time (DST)
190 index to quantify the global reduction in the magnetic field. An example of a DST
191 index time series from the 2015 St. Patrick's Day storm, driven by a coronal mass
192 ejection (CME), is shown in Fig. 1.7. A few notable features of the storm and the
193 ring current are worth pointing out. At the start of the storm the ring current is
194 sometimes depleted and DST increases slightly (termed the initial phase or sudden
195 storm commencement). Then the ring current population is rapidly built up and
196 DST rapidly decreases during the main phase. Lastly, after the storm passes, the
197 ring current gradually decays toward its equilibrium state over a period of a few
198 days and DST returns towards 0 during the recovery phase. The DST index (along
199 with other geomagnetic indices) are readily used by the space physics community to
200 quantify the global state of the magnetosphere.

201 Radiation Belts The highest particle energy populations are in the Van Allen
202 radiation belts. These belts were discovered by Van Allen (1959) and Vernov and
203 Chudakov (1960) during the Cold War and are a pair of toroidally shaped populations
204 of trapped electrons and protons shown in Fig. 1.8. Their quiescent toroidal shape,
205 similar to the shape of the plasmasphere and ring current, is a result of Earth's dipole

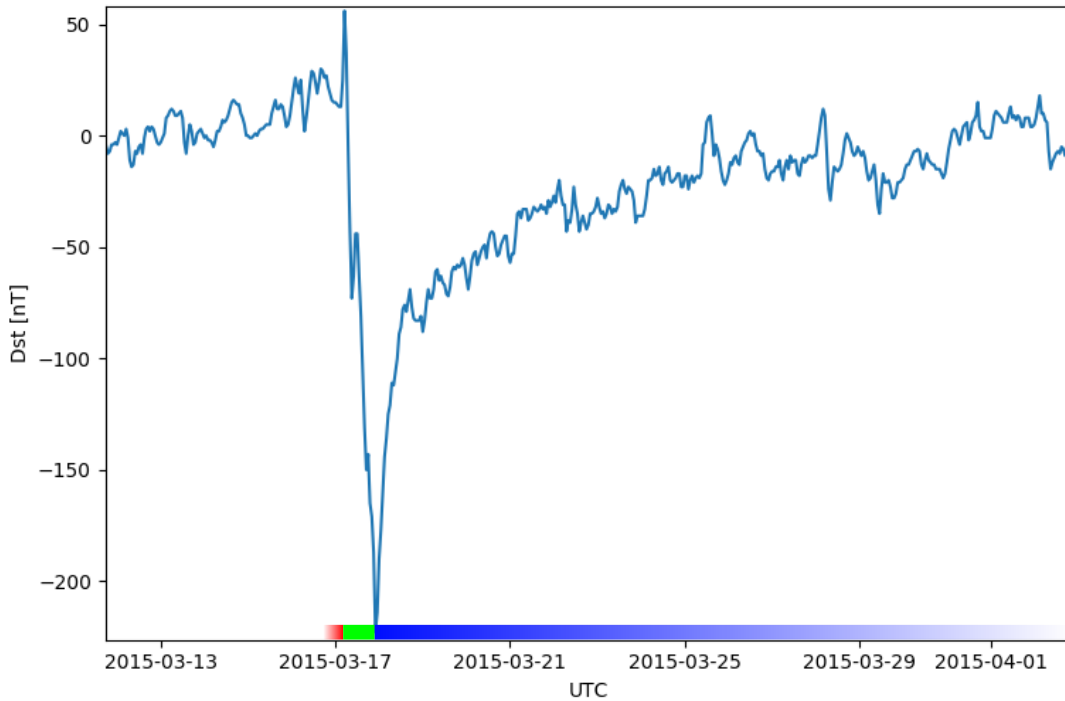


Figure 1.7: The DST index during the St. Patrick's Day 2015 storm. This storm was caused by a coronal mass ejection on March 15th, 2015. The storm phases are: initial phase, main phase, and recovery phase. The initial phase occurred when the Dst peaked at $+50$ nT on March 17th during which the ring current was eroded by the coronal mass ejection during the interval shown by the red bar shown at the bottom. Then the following rapid decrease to ≈ -200 nT was during the main phase where many injections from the magnetotail enhanced the ring current, which reduced Earth's magnetic field strength at the ground, and is shown with the green bar. Lastly, the recovery phase lasted from March 18th to approximately March 29th during which the ring current particles were lost and the ring current returned to its equilibrium state. The recovery phase is shown with the blue bar.

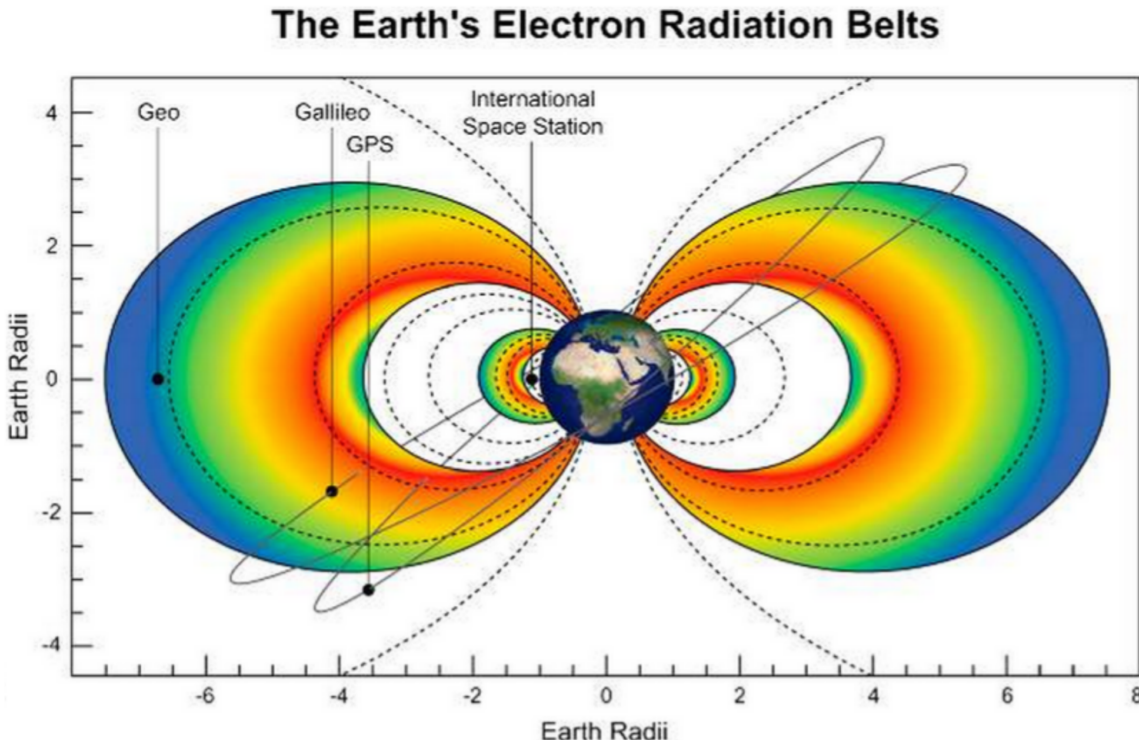


Figure 1.8: The two radiation belts with the locations of various satellites and orbits. Figure from (Horne et al., 2013).

²⁰⁶ magnetic field.

²⁰⁷ The inner radiation belt is extremely stable on time periods of years, extends
²⁰⁸ to $L \approx 2$, and mainly consists of protons with energies between MeV and GeV and
²⁰⁹ electrons with energies up to ≈ 1 MeV (Claudepierre et al., 2019). The source of
²¹⁰ inner radiation belt protons is believed to be due to cosmic-ray albedo neutron decay
²¹¹ (e.g. Li et al., 2017) and inward radial diffusion for electrons (e.g. O'Brien et al.,
²¹² 2016). The gap between the inner and outer radiation belt is called the slot, which is
²¹³ believed to be due to hiss waves inside the plasmasphere (described below) scattering
²¹⁴ particles into the atmosphere (e.g. Breneman et al., 2015; Lyons and Thorne, 1973).

²¹⁵ The outer radiation belt is much more dynamic and consists of mainly electrons
²¹⁶ of energies up to a few MeV. The outer belt's spatial extent is highly variable as

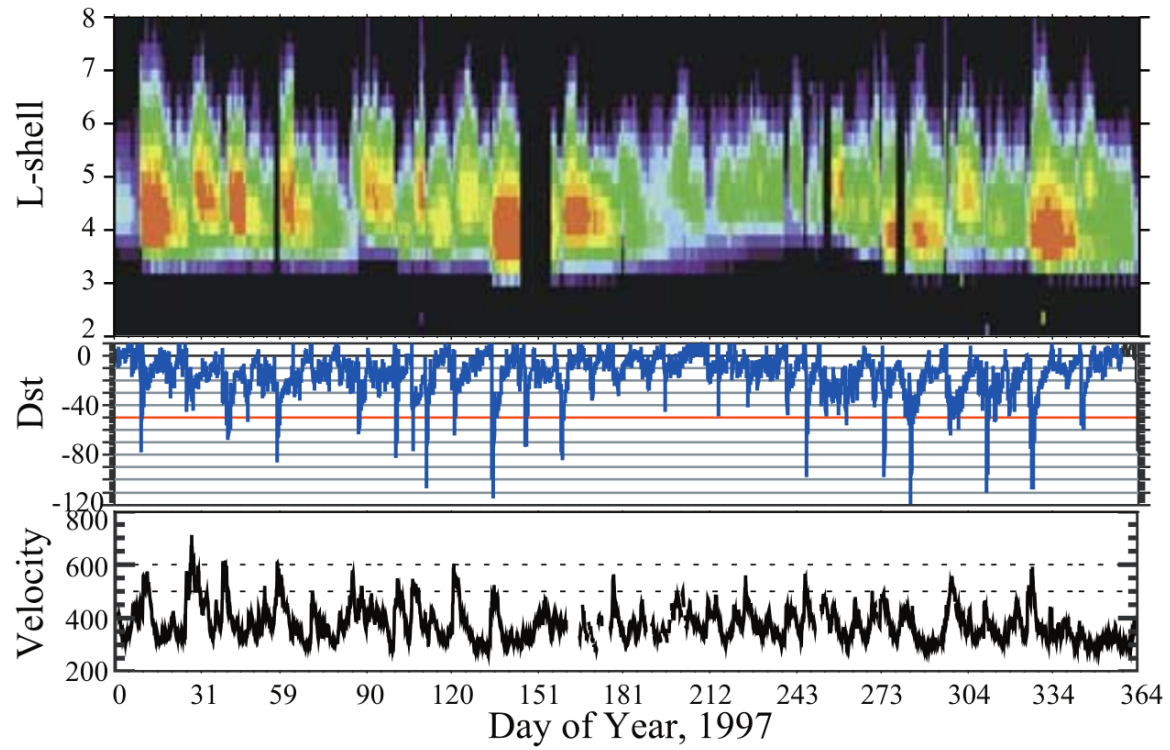


Figure 1.9: The dynamics of the outer radiation belt in 1997 from the POLAR satellite. Top panel shows the 1.2-2.4 MeV electron flux as a function of L and 1997 day of year. The middle panel shows the DST index, and bottom panel shows the solar wind velocity. Figure from (Reeves et al., 2003).

²¹⁷ shown in Fig. 1.9, and is typically observed between L of 4 and 8. The source of
²¹⁸ outer radiation belt electrons is widely believed to be injections of plasma from the
²¹⁹ magnetotail that is then accelerated to high energies.

²²⁰ Due to the highly energetic and dynamic nature of the radiation belts, and their
²²¹ impact on human presence in space, the radiation belts have been studied for over
²²² half century. Researchers have studied and attempted to predict the dynamics of
²²³ radiation belt particles, waves, and wave-particle interactions by considering various
²²⁴ competing particle acceleration and loss mechanisms which are described next.

225

Radiation Belt Particle Sources and Sinks

²²⁶ Adiabatic Heating

²²⁷ One of the particle heating and transport mechanisms arises from the Earthward
²²⁸ convection of particles. The conservation of J_1 implies that the initial and final v_{\perp}
²²⁹ depends on the change in the magnetic field amplitude

$$\frac{v_{\perp i}^2}{B_i} = \frac{v_{\perp f}^2}{B_f}. \quad (1.12)$$

²³⁰ As a particle convets Earthward, $B_f > B_i$ thus v_{\perp} must increase. The dipole
²³¹ magnetic field amplitude can be written as

$$B(L, \theta) = \frac{31.2 \mu\text{T}}{L^3} \sqrt{1 + 3 \cos^2 \theta}. \quad (1.13)$$

²³² The change in v_{\perp}^2 can be found by taking the ratio of $B(L, \theta)$ at two different L shells

$$\frac{v_{\perp f}^2}{v_{\perp i}^2} = \left(\frac{L_i}{L_f} \right)^3 \quad (1.14)$$

²³³ thus the increase in $v_{\perp} \sim (L_i/L_f)^{3/2}$.

234 As the particle convects Earthward its $v_{||}$ also increases because the distance
 235 between the particle's mirror points decrease. If J_2 is conserved, the shrinking bounce
 236 path implies that $v_{||}$ must increase by

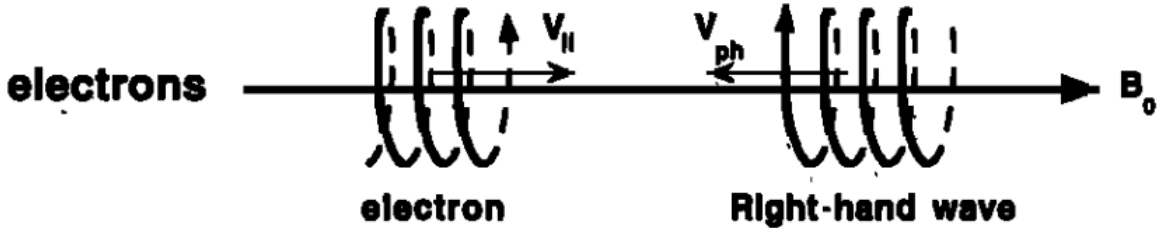
$$\frac{v_{||f}^2}{v_{||i}^2} = \left(\frac{L_i}{L_f}\right)^k \quad (1.15)$$

237 where k ranges from 2 for equatorial pitch angles, $\alpha_{eq} = 0^\circ$, to 2.5 for $\alpha_{eq} = 90^\circ$
 238 (Baumjohann and Treumann, 1997). Since the rate of adiabatic heating is greater in
 239 the perpendicular direction than heating in the parallel direction, an initially isotropic
 240 particle distribution will become anisotropic during its convection. These isotropic
 241 particles can then become unstable to wave growth and generate waves in order to
 242 reach equilibrium.

243 Wave Resonance Heating

244 Another mechanism that heats particles is due to particles resonating with
 245 plasma waves. A few of the electromagnetic wave modes responsible for particle
 246 acceleration (and scattering) relevant to radiation belt dynamics are hiss, whistler
 247 mode chorus (chorus), and electromagnetic ion cyclotron (EMIC) waves. These waves
 248 are created by the loss cone instability that is driven by an anisotropy of electrons for
 249 chorus waves, and protons for EMIC waves. The level of anisotropy can be quantified
 250 by the ratio of the perpendicular to parallel particle temperatures ($T_\perp/T_{||}$). A particle
 251 distribution is unstable when $T_\perp/T_{||} > 1$. Since electrons gyrate in a right-handed
 252 sense, the chorus waves also tend to be right hand circularly polarized (Tsurutani and
 253 Lakhina, 1997). The same argument also applies to protons and left hand circularly
 254 polarized EMIC waves.

255 These circularly polarized waves can resonate with electrons and/or protons
 256 when their relative motion results in a static \vec{E} . One example of a resonance between



$$\omega + k_{\parallel} v_{\parallel} = \Omega^-$$

Figure 1.10: The trajectories of an electron and a right-hand circularly polarized wave during a cyclotron resonance. The electron's v_{\parallel} and the wave's parallel wave vector, k_{\parallel} are in opposite directions such that the wave's frequency is Doppler shifted to an integer multiple of the electron cyclotron frequency. Figure from (Tsurutani and Lakhina, 1997).

257 a right hand circularly polarized wave and an electron is shown in Fig. 1.10. The
 258 electron's v_{\parallel} and the wave's parallel wave vector, k_{\parallel} are in opposite directions such
 259 that the wave frequency ω is Doppler shifted to an integer multiple of the Ω_e where the
 260 electron feels a static electric field and is accelerated or decelerated. Quantitatively,
 261 this resonance condition is easier to understand with the following toy model.

262 Assume a uniform magnetic field $\vec{B} = B_0 \hat{z}$ with a parallel propagating ($k = k \hat{z}$),
 263 right-hand circularly polarized wave. The wave's electric field as a function of position
 264 and time can be written as

$$\vec{E} = E_0 (\cos(\omega t - kz) \hat{x} + \sin(\omega t - kz) \hat{y}). \quad (1.16)$$

The angular component of \vec{E} that will effect the particle's v_{\perp} is

$$E_{\theta} = \vec{E} \cdot \hat{\theta} = E_0 \cos(\omega t - kz + \theta). \quad (1.17)$$

265 Now assume that the electron is traveling in the $-\hat{z}$ direction with a velocity $\vec{v} = -v_0 \hat{z}$

²⁶⁶ so its time dependent position along \hat{z} is

$$z(t) = -v_0 t \quad (1.18)$$

²⁶⁷ and gyrophase is

$$\theta(t) = -\Omega t + \theta(0) \quad (1.19)$$

²⁶⁸ where the first negative sign comes from the electron's negative charge. Now we put
²⁶⁹ this all together and find the force that the electron will experience

$$m \frac{dv_\theta}{dt} = qE_\theta = qE_0 \sin((\omega + kv_0 - \Omega)t + \theta(0)). \quad (1.20)$$

²⁷⁰ This is a relatively complex expression, but when the time dependent component is
²⁷¹ 0, i.e.

$$\omega + kv_0 - \Omega = 0, \quad (1.21)$$

²⁷² the electron will feel a static electric field and be accelerated or decelerated depending
²⁷³ on θ_0 , the phase between the wave and the electron. The expression in Eq. 1.21 is
²⁷⁴ commonly referred to as the resonance condition and is more generally written as

$$\omega - k_{||}v_{||} = \frac{n\Omega_e}{\gamma} \quad (1.22)$$

²⁷⁵ where n is the resonance order, and γ is the relativistic correction (e.g. Millan and
²⁷⁶ Thorne, 2007). In the case of the cyclotron resonance, $\omega \approx \Omega_e$ thus J_1 is violated.
²⁷⁷ Since J_1 is violated, J_2 and J_3 are also violated since the conditions required to violate
²⁷⁸ J_2 and J_3 are less stringent than J_1 . It is important to remember that a particle will
²⁷⁹ experience the effects of many waves along its drift orbit. The typical MLT extent

280 of a handful of waves that are capable of resonating with radiation belt electrons are
 281 shown in Fig. 1.11.

282 Particle Losses

283 Now that we have seen two general mechanisms with which particles are
 284 accelerated in the magnetosphere, we will now consider a few specific mechanisms
 285 that remove particles from the magnetosphere into the atmosphere or the solar
 286 wind. One mechanism that transports magnetosperic particles into the solar wind
 287 is magnetopause shadowing (e.g. Ukhorskiy et al., 2006). Magnetopause shadowing
 288 occurs when the ring current is strengthened and Earth's magnetic field strength is
 289 increased outside of the ring current. If the ring current increases slowly enough (such
 290 that J_3 is conserved), a particle drift shell will move outward to conserve J_3 . If the
 291 particle's drift shell expands past the magnetopause, the particle will be lost to the
 292 solar wind.

293 **Make sure I understand ULF waves and radial diffusion right** Another particle
 294 loss (and acceleration) mechanism is driven by ultra low frequency (ULF) waves and
 295 is called radial diffusion. Radial diffusion is the transport of particles from high
 296 to low phase space density, f . If the transport is radially inward, particles will
 297 appear to be accelerated. On the other hand, radially outward radial diffusion can
 298 transport particles through the magnetopause where they will be lost to the solar
 299 wind. Reeves et al. (2013) investigated the driver of particle acceleration during the
 300 October 2012 storm and observationally found that inward radial diffusion was not
 301 dominant, rather local acceleration via wave-resonance heating appeared to be the
 302 dominant acceleration mechanism.

303 The loss mechanism central to this dissertation is pitch angle and energy
 304 scattering of electrons by waves. Some of the waves that scatter electrons in energy

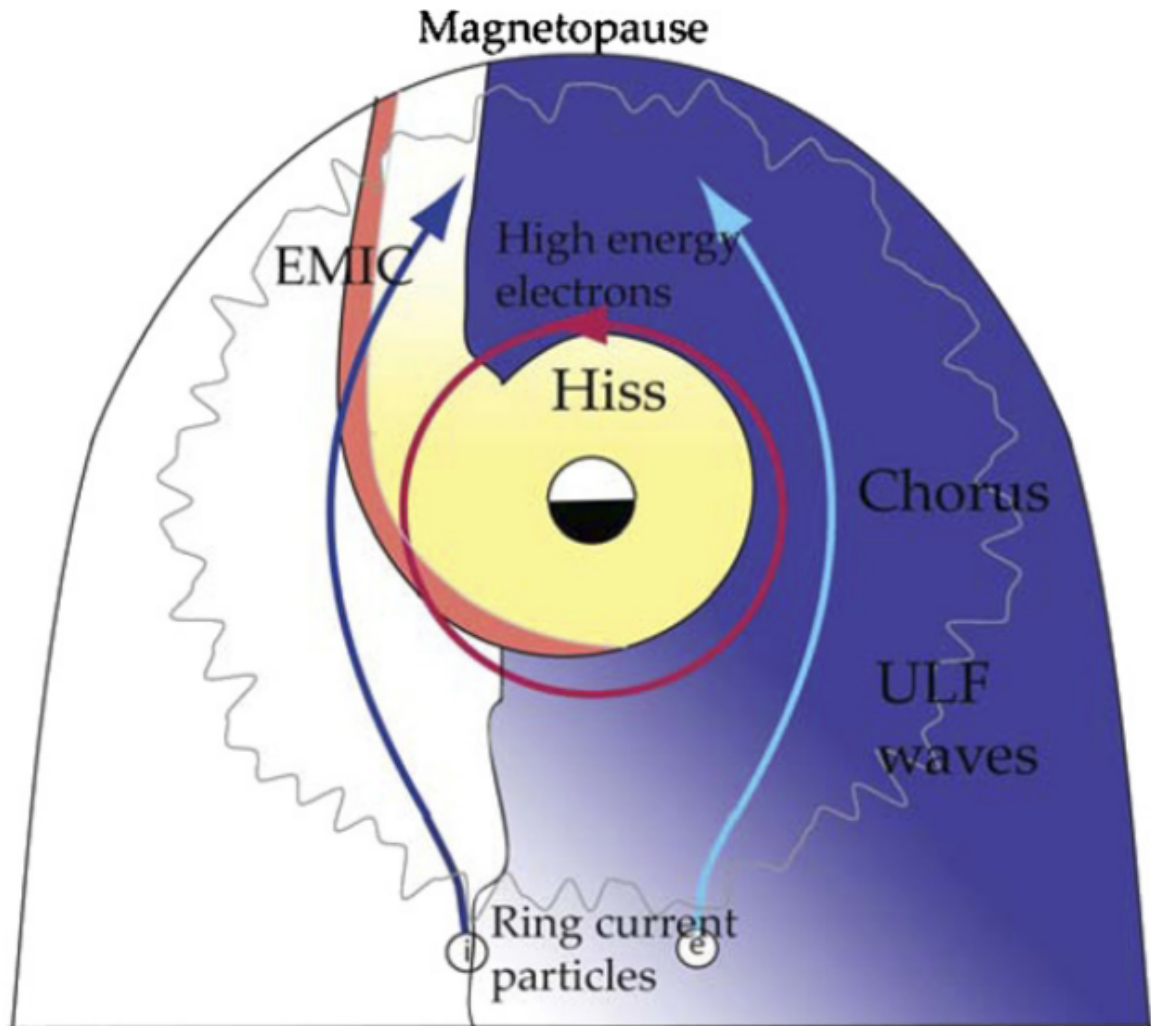


Figure 1.11: Various wave modes in the magnetosphere. Ultra low frequency waves occur through the magnetosphere. Chorus waves are typically observed in the 0-12 midnight-dawn region. EMIC waves are typically observed in the dusk MLT sector. Hiss waves are observed inside the plasmasphere. Figure from Millan and Thorne (2007).

and pitch angle in the inner magnetosphere are: plasmaspheric hiss (e.g. Breneman et al., 2015; O'Brien et al., 2014), EMIC waves (e.g. Capannolo et al., 2019; Hendry et al., 2017), and chorus waves (e.g. Breneman et al., 2017; Kasahara et al., 2018; Ozaki et al., 2019). These wave-particle interactions occur when the resonance condition in Eq. 1.22 is satisfied and the particle's energy and α is modified by the wave. More details regarding the theory of pitch angle and energy diffusion is given in Chapter ???. If the wave changes α towards 0 and $\alpha < \alpha_L$, then the particle's mirror point dips below 100 km altitude where the particle can be lost from the magnetosphere. One manifestation of pitch angle scattering of particles into the loss cone are microbursts: a sub-second durtaison impulse of electrons.

315

Microbursts

Microbursts were first with high altitude balloons which measured bremsstrahlung X-rays emitted by microburst electrons impacting the atmosphere by Anderson and Milton (1964). In the following years, numerous balloon flights expanded our knowledge of non-relativistic (≤ 500 keV) microbursts (relativistic microbursts have not yet been observed by high altitude balloons) by quantifying the microburst spatial extent, temporal width, occurrence frequency, extent in L and MLT, and their source. The microburst source was first believed to be either a local plasma instability or a propagating disturbance in the magnetosphere (Barcus et al., 1966; Brown et al., 1965; Parks, 1967; Trefall et al., 1966). Soon after, both non-relativistic and relativistic microbursts electrons were directly observed in LEO with spacecraft including the Solar Anomalous and Magnetospheric Particle Explorer (SAMPEX) (e.g. Blake et al., 1996; Blum et al., 2015; Douma et al., 2019, 2017; Greeley et al., 2019; Lorentzen et al., 2001a,b; Nakamura et al., 1995, 2000; O'Brien et al., 2004, 2003), Montana State University's (MSU) Focused Investigation of Relativistic Electron Bursts: Intensity,

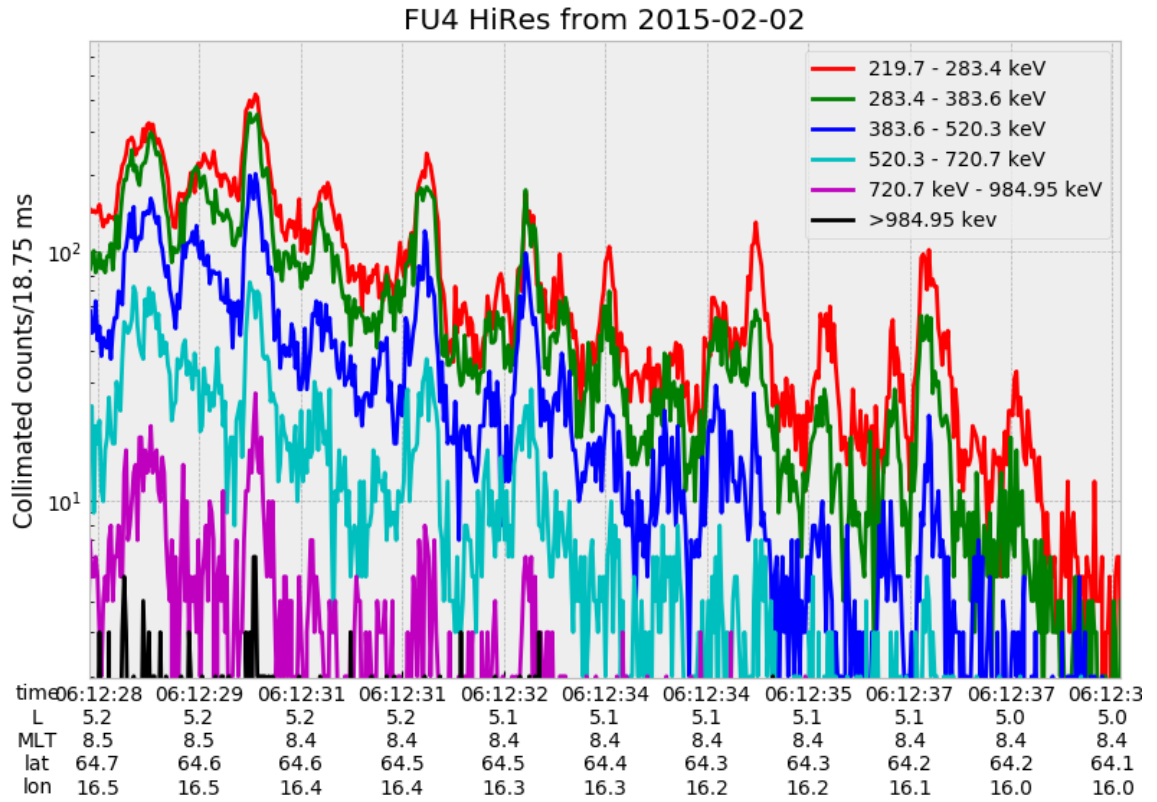


Figure 1.12: An example train of microbursts observed by FIREBIRD-II unit 4 on February 2nd, 2015. The colored curves show the differential energy channel count rates in five channels from ≈ 200 keV to 1 MeV and a sixth integral energy channel with a 1 MeV threshold. The x-axis labels show auxiliary information such as time of observation and the spacecraft position in L, MLT, latitude and longitude coordinates.

330 Range, and Dynamics II (FIREBIRD-II) (Anderson et al., 2017; Breneman et al.,
 331 2017; Crew et al., 2016; Klumpar et al., 2015; Spence et al., 2012), and Science
 332 Technologies Satellite (STSAT-I) (e.g. Lee et al., 2012, 2005). An example microburst
 333 time series is shown in Fig. 1.12 and was observed by the FIREBIRD-II CubeSats.
 334 The prominent features of the example microbursts in Fig. 1.12 are their sub-second
 335 duration, half order of magnitude increase in count rate above the falling background,
 336 and their 200-800 keV energy extent.

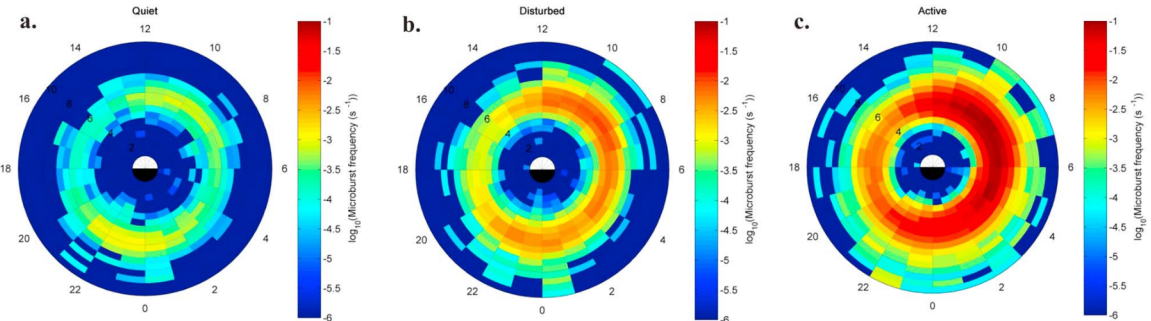


Figure 1.13: Distribution of > 1 MeV microburst occurrence rates as a function of L and MLT. The three panels show the microburst occurrence rate dependence on geomagnetic activity, parameterized by the auroral electrojet (AE) index for (a) $\text{AE} < 100 \text{ nT}$, (b) $100 < \text{AE} < 300 \text{ nT}$ and (c) $\text{AE} > 300 \text{ nT}$. Figure from Douma et al. (2017).

337 Microbursts are observed on magnetic field footprints that are connected to the
 338 outer radiation belt (approximately $4 < L < 8$). They are predominately observed in
 339 the 0-12 MLT sector with an elevated occurrence frequency during magnetospherically
 340 disturbed times as shown in Fig. 1.13 (e.g. Douma et al., 2017). O'Brien et al. (2003)
 341 used SAMPEX relativistic electron data and found that microbursts predominately
 342 occur during the main phase of storms, with a heightened occurrence rate during the
 343 recovery phase. Microburst occurrence rates are also higher during high solar wind
 344 velocity events e.g. from co-rotating interaction regions (Greeley et al., 2019; O'Brien
 345 et al., 2003).

346 The estimated impact of microbursts on the atmosphere and the radiation
 347 belts is significant. Relativistic microburst electrons impacting the atmosphere are
 348 ionized at < 100 km altitudes, with higher energy electrons penetrating closer to
 349 the surface. The resulting chemical reaction of microburst electrons impacting the
 350 atmosphere produces odd hydrogen HO_x and odd nitrogen NO_x molecules, which
 351 are partially responsible for destroying ozone (O_3). Seppälä et al. (2018) modeled
 352 a six hour relativistic microburst storm and found that the mesospheric ozone was

353 reduced by 7 – 12% in the summer months and 12 – 20% in the winter months, so
 354 microbursts may have a non-negligible contribution to the dynamics of atmospheric
 355 ozone. Furthermore, microbursts have also been estimated to have a significant
 356 impact on the outer radiation belt electron population. Radiation belt electron loss
 357 due to microbursts has been estimated to be on the order of a day (Breneman
 358 et al., 2017; Douma et al., 2019; Lorentzen et al., 2001b; O'Brien et al., 2004; Thorne
 359 et al., 2005).

360 The wave-particle interactions responsible for generating microbursts are also
 361 believed to accelerate electrons in the radiation belts. As mentioned earlier, when
 362 an electron is in resonance with a wave, energy is exchanged with the wave and
 363 the electron is either accelerated or decelerated. The signature of wave-particle
 364 acceleration been observed for radiation belt electrons (e.g. Horne et al., 2005;
 365 Meredith et al., 2002; Reeves et al., 2013), and O'Brien et al. (2003) presented evidence
 366 that enhancements in chorus waves, microbursts, and radiation belt electrons are
 367 related. To explain their observations, O'Brien et al. (2003) proposed that microburst
 368 precipitation is a side effect of electron acceleration due to chorus waves.

369 The widely used theoretical framework to model the wave-particle interactions
 370 responsible for accelerating electrons and scattering microbursts is quasi-linear
 371 diffusion (e.g. Horne et al., 2005; Meredith et al., 2002; Summers, 2005; Summers
 372 et al., 1998; Thorne et al., 2005; Walker, 1993). This framework is explained in
 373 Chapter ??, and applied to an observation of a microburst in the heart of the
 374 radiation belt. Qualitatively, when a particle is resonant with a wave it can either
 375 be transported in pitch angle towards the loss cone and lose energy to the wave, or
 376 transported away from the loss cone and gain energy from the wave.

377 As previously mentioned, the range of observed microburst energies range from a
 378 few tens of keV (e.g Datta et al., 1997; Parks, 1967) to greater than 1 MeV (e.g. Blake

³⁷⁹ et al., 1996; Greeley et al., 2019). The microburst electron flux (J) falls off in energy,
³⁸⁰ and the microburst energy spectra is typically well fit to a decaying exponential

$$J(E) = J_0 e^{-E/E_0} \quad (1.23)$$

³⁸¹ where J_0 is the flux at 0 keV (unphysical free parameter) and E_0 quantifies the
³⁸² efficiency of the scattering mechanism in energy (e.g. Datta et al., 1997; Lee et al.,
³⁸³ 2005; Parks, 1967). A small E_0 suggests that mostly low energy particles are scattered.
³⁸⁴ In contrast a high E_0 suggests that the scattering mechanism scatters low and high
³⁸⁵ energy electrons. Reality is a bit more messy and a high E_0 may be a signature of
³⁸⁶ a scattering mechanism preferential to high energy electrons, but is hidden by the
³⁸⁷ convolution of the source particles available to be scattered (typically with a falling
³⁸⁸ energy spectrum) and the energy-dependent efficiency of the scattering mechanism.

³⁸⁹ The short microburst duration observed by a single LEO satellite has an
³⁹⁰ ambiguity when interpreting what is exactly a microburst. The two possible realities
³⁹¹ are: a microburst is very small and spatially stationary so that the LEO spacecraft
³⁹² passes through it in less than a second. Alternatively, microbursts are spatially large
³⁹³ and transient so a microburst will pass by the spacecraft in a fraction of a second.
³⁹⁴ There are a few ways to distinguish between the two possible realities, and each one
³⁹⁵ has a unique set of advantages.

³⁹⁶ A high altitude balloon provides essentially a stationary view of the precipitating
³⁹⁷ particles under the radiation belt footprints. A short-lived, temporal microburst can
³⁹⁸ be unambiguously identified. Spatial structures, on the other hand, are difficult to
³⁹⁹ identify because a balloon is essentially still on drift timescales.

⁴⁰⁰ Multi-spacecraft missions are an alternate solution that can determine if a
⁴⁰¹ microburst is spatial or temporal. As will be shown in this dissertation, if a microburst

402 is observed simultaneously by two spacecraft then it is temporal and has a size
403 greater than the spacecraft separation. On the contrary, if two spacecraft observe
404 a microburst-like feature at different times but at the same location, then the feature
405 is spatial and may be a curtain (Blake and O'Brien, 2016). Both balloon and multi-
406 spacecraft observational methods have a unique set of strengths, and this dissertation
407 takes the multi-spacecraft approach to identify and study microbursts.

408

Scope of Reserach

409 This dissertation furthers our understanding of the microburst scattering
410 mechanism by presenting observational evidence of microburst scattering directly, and
411 measuring microburst sizes and comparing them to the size of chorus waves. Chapter
412 ?? describes a microburst scattering event observed by NASA's Van Allen Probes.
413 For this event, particle and wave measurements were analyzed and modeled in the
414 theoretical framework of pitch angle and energy diffusion. Then the following two
415 chapters present studies of microburst sizes in comparison to chorus waves. Chapter
416 ?? describes a bouncing packet microburst observation made by the FIREBIRD-II
417 mission where the microburst's lower bound longitudinal and latitudinal sizes were
418 estimated. Then Chapter ?? expands the case study from Chapter ?? to a statistical
419 study of microburst sizes using The Aerospace Corporation's AeroCube-6 (AC6)
420 CubeSats. In this study, a Monte Carlo and analytic microburst size models were
421 developed to account for the compounding statistical effects of random microburst
422 sizes and locations. Lastly, Chapter ?? will summarize this work and make concluding
423 remarks regarding outstanding questions in microburst physics.

Bibliography

- 425 Anderson, B., Shekhar, S., Millan, R., Crew, A., Spence, H., Klumpar, D., Blake, J.,
 426 O'Brien, T., and Turner, D. (2017). Spatial scale and duration of one microburst
 427 region on 13 August 2015. *Journal of Geophysical Research: Space Physics*.
- 428 Anderson, K. A. and Milton, D. W. (1964). Balloon observations of X rays in the
 429 auroral zone: 3. High time resolution studies. *Journal of Geophysical Research*,
 430 69(21):4457–4479.
- 431 Barcus, J., Brown, R., and Rosenberg, T. (1966). Spatial and temporal character of
 432 fast variations in auroral-zone x rays. *Journal of Geophysical Research*, 71(1):125–
 433 141.
- 434 Baumjohann, W. and Treumann, R. A. (1997). *Basic space plasma physics*. World
 435 Scientific.
- 436 Blake, J.,Looper, M., Baker, D., Nakamura, R., Klecker, B., and Hovestadt, D.
 437 (1996). New high temporal and spatial resolution measurements by sampex of the
 438 precipitation of relativistic electrons. *Advances in Space Research*, 18(8):171 – 186.
- 439 Blake, J. B. and O'Brien, T. P. (2016). Observations of small-scale latitudinal
 440 structure in energetic electron precipitation. *Journal of Geophysical Research: Space
 441 Physics*, 121(4):3031–3035. 2015JA021815.
- 442 Blum, L., Li, X., and Denton, M. (2015). Rapid MeV electron precipitation as
 443 observed by SAMPEX/HILT during high-speed stream-driven storms. *Journal of
 444 Geophysical Research: Space Physics*, 120(5):3783–3794. 2014JA020633.
- 445 Breneman, A., Crew, A., Sample, J., Klumpar, D., Johnson, A., Agapitov, O.,
 446 Shumko, M., Turner, D., Santolik, O., Wygant, J., et al. (2017). Observations
 447 directly linking relativistic electron microbursts to whistler mode chorus: Van allen
 448 probes and FIREBIRD II. *Geophysical Research Letters*.
- 449 Breneman, A. W., Halford, A., Millan, R., McCarthy, M., Fennell, J., Sample, J.,
 450 Woodger, L., Hospodarsky, G., Wygant, J. R., Cattell, C. A., et al. (2015). Global-
 451 scale coherence modulation of radiation-belt electron loss from plasmaspheric hiss.
 452 *Nature*, 523(7559):193.
- 453 Brown, R., Barcus, J., and Parsons, N. (1965). Balloon observations of auroral zone
 454 x rays in conjugate regions. 2. microbursts and pulsations. *Journal of Geophysical
 455 Research (U.S.)*.
- 456 Capannolo, L., Li, W., Ma, Q., Shen, X.-C., Zhang, X.-J., Redmon, R., Rodriguez,
 457 J., Engebretson, M., Kletzing, C., Kurth, W., et al. (2019). Energetic electron
 458 precipitation: multi-event analysis of its spatial extent during emic wave activity.
 459 *Journal of Geophysical Research: Space Physics*.

- 460 Claudepierre, S., O'Brien, T.,Looper, M., Blake, J., Fennell, J., Roeder, J.,
 461 Clemmons, J., Mazur, J., Turner, D., Reeves, G., et al. (2019). A revised look
 462 at relativistic electrons in the earth's inner radiation zone and slot region. *Journal*
 463 *of Geophysical Research: Space Physics*, 124(2):934–951.
- 464 Crew, A. B., Spence, H. E., Blake, J. B., Klumpar, D. M., Larsen, B. A., O'Brien,
 465 T. P., Driscoll, S., Handley, M., Legere, J., Longworth, S., Mashburn, K.,
 466 Mosleh, E., Ryhajlo, N., Smith, S., Springer, L., and Widholm, M. (2016). First
 467 multipoint in situ observations of electron microbursts: Initial results from the
 468 NSF FIREBIRD II mission. *Journal of Geophysical Research: Space Physics*,
 469 121(6):5272–5283. 2016JA022485.
- 470 Datta, S., Skoug, R., McCarthy, M., and Parks, G. (1997). Modeling of microburst
 471 electron precipitation using pitch angle diffusion theory. *Journal of Geophysical*
 472 *Research: Space Physics*, 102(A8):17325–17333.
- 473 Douma, E., Rodger, C., Blum, L., O'Brien, T., Clilverd, M., and Blake, J. (2019).
 474 Characteristics of relativistic microburst intensity from sampex observations.
 475 *Journal of Geophysical Research: Space Physics*.
- 476 Douma, E., Rodger, C. J., Blum, L. W., and Clilverd, M. A. (2017). Occurrence
 477 characteristics of relativistic electron microbursts from SAMPEX observations.
 478 *Journal of Geophysical Research: Space Physics*, 122(8):8096–8107. 2017JA024067.
- 479 Eastwood, J., Hietala, H., Toth, G., Phan, T., and Fujimoto, M. (2015). What
 480 controls the structure and dynamics of earths magnetosphere? *Space Science*
 481 *Reviews*, 188(1-4):251–286.
- 482 Fang, X., Randall, C. E., Lummerzheim, D., Wang, W., Lu, G., Solomon, S. C., and
 483 Frahm, R. A. (2010). Parameterization of monoenergetic electron impact ionization.
 484 *Geophysical Research Letters*, 37(22).
- 485 Greeley, A., Kanekal, S., Baker, D., Klecker, B., and Schiller, Q. (2019). Quantifying
 486 the contribution of microbursts to global electron loss in the radiation belts. *Journal*
 487 *of Geophysical Research: Space Physics*.
- 488 Hendry, A. T., Rodger, C. J., and Clilverd, M. A. (2017). Evidence of sub-mev
 489 emic-driven electron precipitation. *Geophysical Research Letters*, 44(3):1210–1218.
- 490 Horne, R., Glauert, S., Meredith, N., Boscher, D., Maget, V., Heynderickx, D., and
 491 Pitchford, D. (2013). Space weather impacts on satellites and forecasting the earth's
 492 electron radiation belts with spacecast. *Space Weather*, 11(4):169–186.
- 493 Horne, R. B., Thorne, R. M., Shprits, Y. Y., Meredith, N. P., Glauert, S. A., Smith,
 494 A. J., Kanekal, S. G., Baker, D. N., Engebretson, M. J., Posch, J. L., et al.
 495 (2005). Wave acceleration of electrons in the van allen radiation belts. *Nature*,
 496 437(7056):227.

- 497 Kasahara, S., Miyoshi, Y., Yokota, S., Mitani, T., Kasahara, Y., Matsuda, S.,
 498 Kumamoto, A., Matsuoka, A., Kazama, Y., Frey, H., et al. (2018). Pulsating
 499 aurora from electron scattering by chorus waves. *Nature*, 554(7692):337.
- 500 Klumper, D., Springer, L., Mosleh, E., Mashburn, K., Berardinelli, S., Gunderson,
 501 A., Handly, M., Ryhajlo, N., Spence, H., Smith, S., Legere, J., Widholm, M.,
 502 Longworth, S., Crew, A., Larsen, B., Blake, J., and Walmsley, N. (2015). Flight
 503 system technologies enabling the twin-cubesat firebird-ii scientific mission.
- 504 Lee, J. J., Parks, G. K., Lee, E., Tsurutani, B. T., Hwang, J., Cho, K. S., Kim, K.-H.,
 505 Park, Y. D., Min, K. W., and McCarthy, M. P. (2012). Anisotropic pitch angle
 506 distribution of 100 keV microburst electrons in the loss cone: measurements from
 507 STSAT-1. *Annales Geophysicae*, 30(11):1567–1573.
- 508 Lee, J.-J., Parks, G. K., Min, K. W., Kim, H. J., Park, J., Hwang, J., McCarthy,
 509 M. P., Lee, E., Ryu, K. S., Lim, J. T., Sim, E. S., Lee, H. W., Kang, K. I., and
 510 Park, H. Y. (2005). Energy spectra of 170–360 keV electron microbursts measured
 511 by the korean STSAT-1. *Geophysical Research Letters*, 32(13). L13106.
- 512 Li, X., Selesnick, R., Schiller, Q., Zhang, K., Zhao, H., Baker, D. N., and Temerin,
 513 M. A. (2017). Measurement of electrons from albedo neutron decay and neutron
 514 density in near-earth space. *Nature*, 552(7685):382.
- 515 Lorentzen, K. R., Blake, J. B., Inan, U. S., and Bortnik, J. (2001a). Observations
 516 of relativistic electron microbursts in association with VLF chorus. *Journal of
 517 Geophysical Research: Space Physics*, 106(A4):6017–6027.
- 518 Lorentzen, K. R., Looper, M. D., and Blake, J. B. (2001b). Relativistic electron
 519 microbursts during the GEM storms. *Geophysical Research Letters*, 28(13):2573–
 520 2576.
- 521 Lyons, L. R. and Thorne, R. M. (1973). Equilibrium structure of radiation belt
 522 electrons. *Journal of Geophysical Research*, 78(13):2142–2149.
- 523 Meredith, N., Horne, R., Summers, D., Thorne, R., Iles, R., Heynderickx, D., and
 524 Anderson, R. (2002). Evidence for acceleration of outer zone electrons to relativistic
 525 energies by whistler mode chorus. In *Annales Geophysicae*, volume 20, pages 967–
 526 979.
- 527 Millan, R. and Thorne, R. (2007). Review of radiation belt relativistic electron losses.
 528 *Journal of Atmospheric and Solar-Terrestrial Physics*, 69(3):362 – 377.
- 529 Nakamura, R., Baker, D. N., Blake, J. B., Kanekal, S., Klecker, B., and Hovestadt,
 530 D. (1995). Relativistic electron precipitation enhancements near the outer edge of
 531 the radiation belt. *Geophysical Research Letters*, 22(9):1129–1132.

- 532 Nakamura, R., Isowa, M., Kamide, Y., Baker, D., Blake, J., and Looper, M. (2000).
 533 Observations of relativistic electron microbursts in association with VLF chorus.
 534 *J. Geophys. Res.*, 105:15875–15885.
- 535 O'Brien, T., Claudepierre, S., Blake, J., Fennell, J. F., Clemmons, J., Roeder, J.,
 536 Spence, H. E., Reeves, G., and Baker, D. (2014). An empirically observed pitch-
 537 angle diffusion eigenmode in the earth's electron belt near $\text{L}^* = 5.0$. *Geophysical*
 538 *Research Letters*, 41(2):251–258.
- 539 O'Brien, T., Claudepierre, S., Guild, T., Fennell, J., Turner, D., Blake, J., Clemmons,
 540 J., and Roeder, J. (2016). Inner zone and slot electron radial diffusion revisited.
 541 *Geophysical Research Letters*, 43(14):7301–7310.
- 542 O'Brien, T. and Moldwin, M. (2003). Empirical plasmapause models from magnetic
 543 indices. *Geophysical Research Letters*, 30(4).
- 544 O'Brien, T. P., Looper, M. D., and Blake, J. B. (2004). Quantification of relativistic
 545 electron microburst losses during the GEM storms. *Geophysical Research Letters*,
 546 31(4). L04802.
- 547 O'Brien, T. P., Lorentzen, K. R., Mann, I. R., Meredith, N. P., Blake, J. B., Fennell,
 548 J. F., Looper, M. D., Milling, D. K., and Anderson, R. R. (2003). Energization of
 549 relativistic electrons in the presence of ULF power and MeV microbursts: Evidence
 550 for dual ULF and VLF acceleration. *Journal of Geophysical Research: Space*
 551 *Physics*, 108(A8).
- 552 Ozaki, M., Miyoshi, Y., Shiokawa, K., Hosokawa, K., Oyama, S.-i., Kataoka, R.,
 553 Ebihara, Y., Ogawa, Y., Kasahara, Y., Yagitani, S., et al. (2019). Visualization of
 554 rapid electron precipitation via chorus element wave–particle interactions. *Nature*
 555 *communications*, 10(1):257.
- 556 Parks, G. K. (1967). Spatial characteristics of auroral-zone X-ray microbursts. *Journal*
 557 *of Geophysical Research*, 72(1):215–226.
- 558 Reeves, G., Spence, H. E., Henderson, M., Morley, S., Friedel, R., Funsten, H., Baker,
 559 D., Kanekal, S., Blake, J., Fennell, J., et al. (2013). Electron acceleration in the
 560 heart of the van allen radiation belts. *Science*, 341(6149):991–994.
- 561 Reeves, G. D., McAdams, K. L., Friedel, R. H. W., and O'Brien, T. P. (2003). Ac-
 562 celeration and loss of relativistic electrons during geomagnetic storms. *Geophysical*
 563 *Research Letters*, 30(10):n/a–n/a. 1529.
- 564 Schulz, M. and Lanzerotti, L. J. (1974). *Particle Diffusion in the Radiation Belts*.
 565 Springer.

- 566 Seppälä, A., Douma, E., Rodger, C., Verronen, P., Clilverd, M. A., and Bortnik, J.
 567 (2018). Relativistic electron microburst events: Modeling the atmospheric impact.
 568 *Geophysical Research Letters*, 45(2):1141–1147.
- 569 Spence, H. E., Blake, J. B., Crew, A. B., Driscoll, S., Klumpar, D. M., Larsen,
 570 B. A., Legere, J., Longworth, S., Mosleh, E., O'Brien, T. P., Smith, S., Springer,
 571 L., and Widholm, M. (2012). Focusing on size and energy dependence of electron
 572 microbursts from the van allen radiation belts. *Space Weather*, 10(11).
- 573 Summers, D. (2005). Quasi-linear diffusion coefficients for field-aligned electro-
 574 magnetic waves with applications to the magnetosphere. *Journal of Geophysical
 575 Research: Space Physics*, 110(A8):n/a–n/a. A08213.
- 576 Summers, D., Thorne, R. M., and Xiao, F. (1998). Relativistic theory of wave-particle
 577 resonant diffusion with application to electron acceleration in the magnetosphere.
 578 *Journal of Geophysical Research: Space Physics*, 103(A9):20487–20500.
- 579 Thorne, R. M., O'Brien, T. P., Shprits, Y. Y., Summers, D., and Horne, R. B. (2005).
 580 Timescale for MeV electron microburst loss during geomagnetic storms. *Journal
 581 of Geophysical Research: Space Physics*, 110(A9). A09202.
- 582 Trefall, H., Bjordal, J., Ullaland, S., and Stadsnes, J. (1966). On the extension of
 583 auroral-zone x-ray microbursts. *Journal of Atmospheric and Terrestrial Physics*,
 584 28(2):225–233.
- 585 Tsurutani, B. T. and Lakhina, G. S. (1997). Some basic concepts of wave-particle
 586 interactions in collisionless plasmas. *Reviews of Geophysics*, 35(4):491–501.
- 587 Ukhorskiy, A. Y., Anderson, B. J., Brandt, P. C., and Tsyganenko, N. A. (2006).
 588 Storm time evolution of the outer radiation belt: Transport and losses. *Journal of
 589 Geophysical Research: Space Physics*, 111(A11):n/a–n/a. A11S03.
- 590 Van Allen, J. A. (1959). The geomagnetically trapped corpuscular radiation. *Journal
 591 of Geophysical Research*, 64(11):1683–1689.
- 592 Vernov, S. and Chudakov, A. (1960). Investigation of radiation in outer space. In
 593 *International Cosmic Ray Conference*, volume 3, page 19.
- 594 Walker, A. D. M. (1993). *Plasma waves in the magnetosphere*, volume 24. Springer
 595 Science & Business Media.